Quad-channel waveguide-based near-eye display for metaverse

Chao Ping Chen [a,*], Xinyu Ma [a], Seak Pang Zou [a], Tingyu Liu [a], Qiang Chu [a], Haiyang Hu [a], Yuepeng Cui [b]

[a] Smart Display Lab, Department of Electronic Engineering, Shanghai Jiao Tong University, Shanghai, China
[b] InfoTek Information Science & Technology Co., Ltd., Shanghai, China

ARTICLE INFO

ABSTRACT

We present a quad-channel waveguide-based near-eye display as an ultra-wide-angle architecture for the metaverse. The core concept is to divide one field of view into four by placing the couplers within the regions, where only the subsets of field of view are located. Compared to its counterparts, including the single-, double- and triple- channels, our quad-channel waveguide can push the envelope of field of view further. With the aid of k-space diagram, the upper limit of field of view is illustrated and deduced. The design rules of the waveguide, sawtooth grating as the in-coupler, and slanted grating as the out-coupler are expounded. Through the rigorous coupled-wave analysis, the diffraction efficiencies of gratings can be calculated and optimized. As an overall evaluation, its key performance indicators are summarized as follows. Field of view is 100° (diagonal), eye relief is 10 mm, exit pupil is 11.5×11.5 mm^2, average transmittance is 2.56 %, and average uniformity is 75 %.

1. Introduction

Metaverse—a portmanteau of "meta" (beyond or transcending) and "universe"—has been getting a plethora of press coverage since Facebook rebranded itself as Meta in October of 2021. However, sometimes, with great hope comes great disappointment. For the past two years, the global market for the metaverse hardware—commonly known as augmented/virtual reality (AR/VR) headsets—was weaker than expected [1]. Putting the macroeconomic reasons aside, the lack of breakthrough in the hardware is largely to blame. Of all hardware components, near-eye display (NED) is probably the one that needs to be improved the most. Of all types of NEDs, the magnifier-based NEDs [2–4] for VR headsets are holding a dominant position, accounting for more than 99 % of the market share. This is mostly due to two reasons. First, the magnifiers are simple in structure and low in cost. Second, they are able to offer big field of views (FOVs). For instance, the FOV of Oculus Quest 2 is 114° (96° (horizontal or H) × 94° (vertical or V)) [5]. Despite seeming invincible, this type of NEDs does have an Achilles' heel, i.e., the bulky form factor. For wearable devices, the form factor could be a deal breaker for many consumers. And even worse, a curve or corner for other types of NEDs to overtake.

Impossible as it may sound, the waveguide-based NEDs [6–16] are manifesting such ambition. While the early waveguide-based NEDs were often criticized for their small FOVs, the recent studies [17–20] had pointed out that the upper limit of FOV could be significantly elevated by the FOV division techniques. In 2016, Vallius et al. (Microsoft) patented a butterfly-like grating pattern to divide one FOV into two [17]. In 2018, Capasso et al. (Harvard University) reformed the above idea by using the polarization-dependent gratings [18]. In 2020, Lee et al. (Seoul National University) introduced a variant of FOV division by time-division multiplexing [19]. In 2022, our group managed to split one FOV into three with a triple-channel waveguide [20]. Inspired by the formers and to step up the game, we hereby present a quad-channel waveguide-based NED, whose FOV can be on par with those of magnifier-based NEDs. In the subsequent sections, we will be going through its design, principles, and key performance indicators.

2. Design rules

2.1. Regions of FOVs

By definition, FOV is an angular size of the image of microdisplay. For waveguide-based NEDs, whose virtual image distance is infinite, it is required that light be collimated. Under such circumstance, the FOV will be determined by the size of microdisplay M and focal length of lens f as [21]

$$FOV = 2tan^{-1}\left(\frac{M}{2f}\right) \tag{1}$$

Now consider a microdisplay consisting of 4 areas, which are colored in red/orange/green/blue, respectively, as in Fig. 1. Accordingly, the FOV of entire microdisplay can be subdivided into $FOV_{1/2/3/4}$. After drawing out the rays of boundaries of each area, the regions of FOV, $FOV_{1/2/3/4}$ and other combinations could then be identified by filling them with distinct colors. There are a total of 10 such regions. Customarily, optical designers are only interested in the region of FOV since this is where all four sub-FOVs are superimposed [22]. But in our case, for which the FOV is not coupled in and out as a whole, it is the regions of $FOV_{1/2/3/4}$ that are of interest to us. This paradigm shift in the choice of regions of FOVs is particularly beneficial to waveguide-based NEDs. The greatest benefit of doing so is that the number of divisions of FOV could be as many as we want, which is not possible with the said FOV division techniques [17–20].

2.2. Quad-channel waveguide

Fig. 2 shows a cross-section of the proposed quad-channel waveguide, with its four layers being referred to as channel 1/2/3/4. As previously mentioned, in-coupling gratings (ICGs) are placed within the regions of $FOV_{1/2/3/4}$ such that four sub-FOVs shall be coupled into their respective channels. The salient feature of this arrangement is that the ICGs are misaligned, making them look quite different from the traditional way. In order for the field angles after in-coupling to be equal, the tilt angles $\theta_{1/2/3/4}$ of ICGs shall be adjusted. Out-coupling gratings (OCGs), on the other side, shall be tilted by the same angles but towards the opposite direction. In this manner, four sub-FOVs could be recombined into the original one. To guarantee a big FOV, a lanthanum dense flint glass N-LASF31 (Schott) is chosen as the material of waveguide, whose refractive index n_{wg} at 633/546/486 nm is 1.8762/1.8858/1.8958, yielding to a critical angle θ_c of 32.22°/32.03°/31.85°.

2.3. Upper limit of FOV

Without loss of generality and to avoid excess notations, we prefer to exemplify with a one-dimensional scenario, wherein the FOV is divided merely along the horizontal direction. As shown in Fig. 3, the transport of FOV from air to waveguide can be interpreted by means of the wave vector space or k-space—a Cartesian coordinate formed by the x-component (k_x) and y-component (k_y) of wave vectors [23]. Usually, the k-space diagram comes with two circles to define the borders of wave vectors in air (inner circle) and waveguide (outer circle). As the microdisplay is rectangular, the area of its FOV in air will be maximized when its aspect ratio becomes 1. By equating the vertical FOV (FOV_v) to horizontal FOV (FOV_h), FOV in air could be simplified as

$$FOV = 2tan^{-1}\left(\sqrt{2}\,tan\left(\frac{FOV_h}{2}\right)\right) \tag{2}$$

After entering into the waveguide, all sub-FOVs are supposed to be overlapped and tangent or adjacent to the inner circle. Obviously, the minimal angle of FOV_h in waveguide is the critical angle θ_c. To enable the exit pupil expansion, there shall exist a maximal angle θ_{max} of FOV_h in waveguide [23], which can be written as

$$\theta_{max} = tan^{-1}\left(\frac{W_{out}}{2DN_{min}}\right) \tag{3}$$

where W_{out} is the width of OCG, D the waveguide thickness, and N_{min} the minimally required number of pupils. By converting the FOV_h from waveguide to air, the maximum FOV_h or FOV_{hmax} shall be

$$FOV_{hmax} = 2sin^{-1}\left(\frac{n_{wg}}{n_{air}}sin\left(\frac{N_c(\theta_{max}-\theta_c)}{2}\right)\right) \tag{4}$$

where n_{air} is the refractive index of air, and N_c the number of channels, by which FOV is divided. Provided $W_{out} = 30$ mm, $D = 1.6$ mm, $N_{min} = 10$, and $m = 1/2/3/4$, and by substituting FOV_{hmax} into Eq. (2), the upper limit of FOV can be calculated with respect to the refractive index of waveguide, as shown in Fig. 4. When $n_{wg} = 1.8858$, the upper limit of FOV is 29°/58°/85°/110° for the single/dual/triple/quad-channel waveguide.

2.4. In-coupling grating

In order for the ICG to be high-efficiency, wide-band, and wide-angle, we resort to the sawtooth or blazed grating for such purposes,
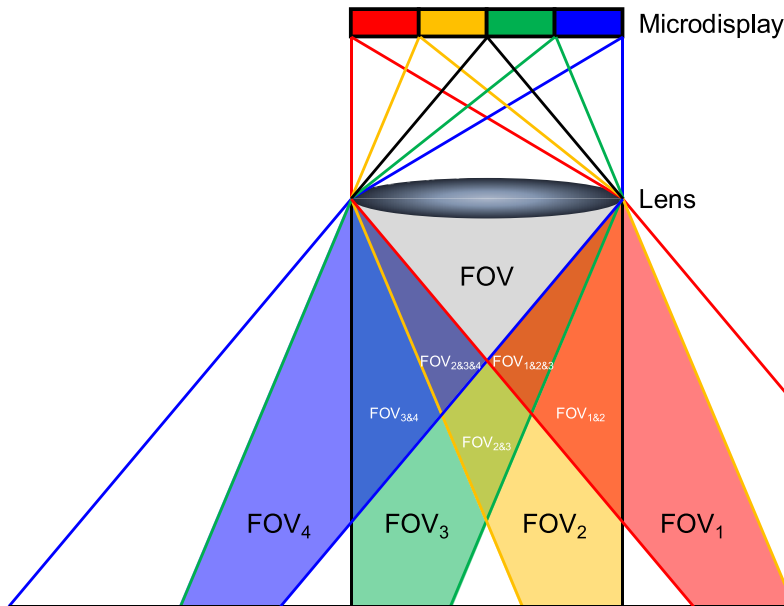

Fig. 1. Consider a microdisplay consisting of 4 areas, which are colored in red/orange/green/blue, respectively. Accordingly, the FOV of entire microdisplay can be subdivided into $FOV_{1/2/3/4}$. After drawing out the rays of boundaries of each area, the regions of FOV, $FOV_{1/2/3/4}$ and other combinations could then be identified by filling them with distinct colors.
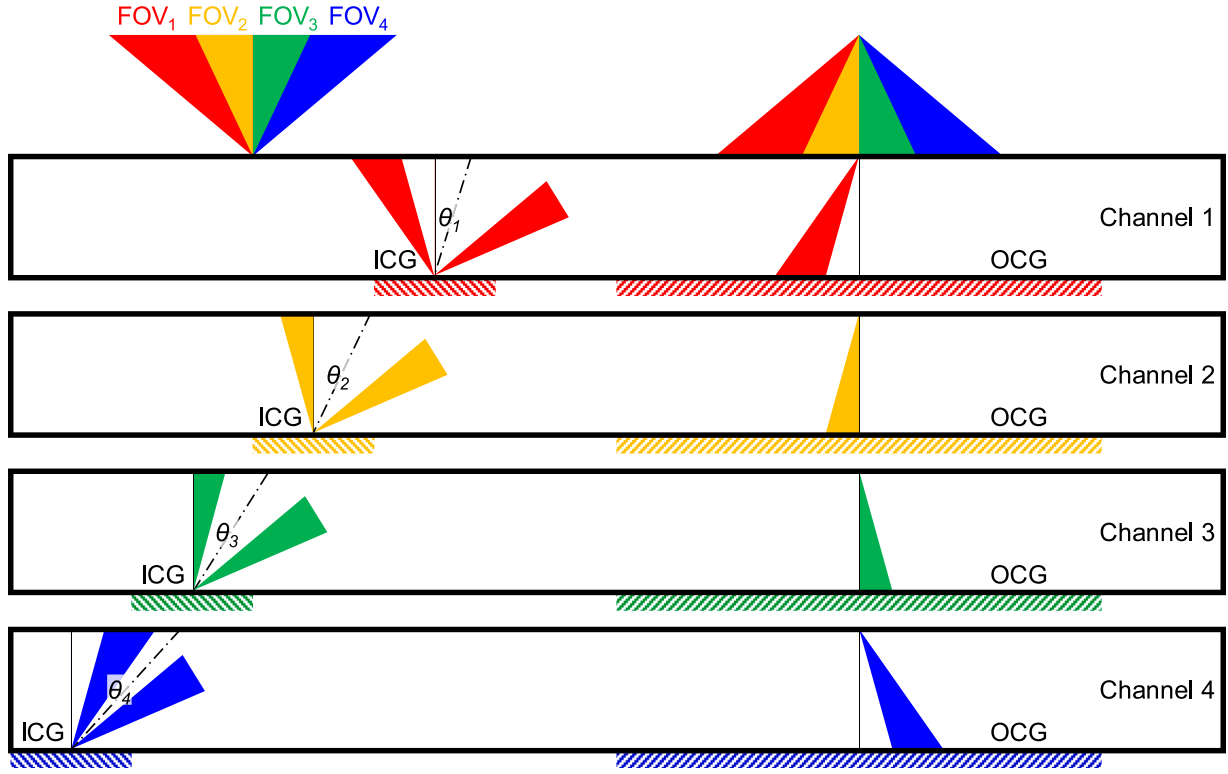
Fig. 2. Cross-section view of quad-channel waveguide. ICGs are placed within the regions of FOV$_{1/2/3/4}$ such that four sub-FOVs shall be coupled into their respective channels. In order for the field angles after in-coupling to be equal, the tilt angles $\theta_{1/2/3/4}$ of ICGs shall be adjusted. OCGs, on the other side, shall be tilted by the same angles but towards the opposite direction. In this manner, four sub-FOVs could be recombined into the original one.
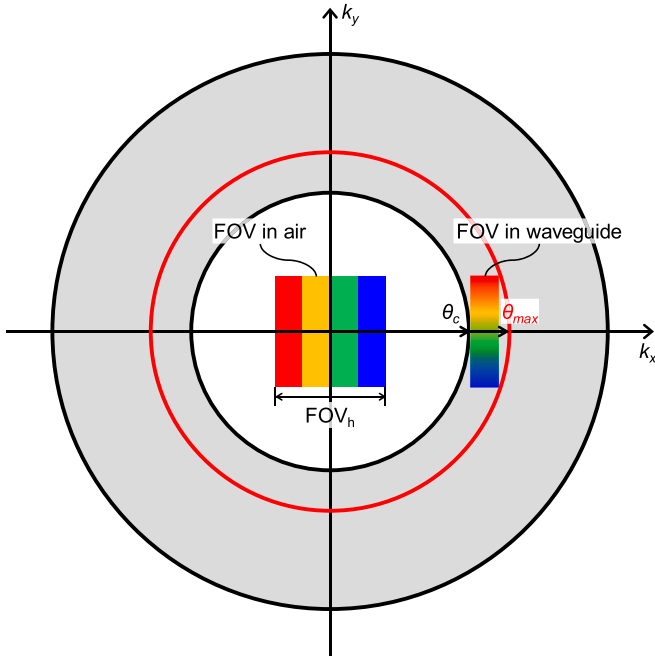

Fig. 3. Transport of FOV from air to waveguide can be interpreted by means of the wave vector space or k-space—a Cartesian coordinate formed by the x-component (k_x) and y-component (k_y) of wave vectors.

as shown in Fig. 5. Pursuant to the grating equation [24], the incident angle θ_i, reflected angle θ_r of the first order, grating period p_i, wavelength λ, and refractive index of waveguide n_{wg} could be correlated via

$$p_i(sin\theta_i - sin\theta_r) = \frac{\lambda}{n_{wg}} \tag{5}$$

Moreover, θ_i, θ_r, and the tilt angle $\theta_{1/2/3/4}$ of ICG or the grating normal also satisfy

$$\theta_{1/2/3/4} = \frac{\theta_i + \theta_r}{2} = tan^{-1}\left(\frac{h_i}{p_i}\right) \tag{6}$$

where h_i is the grating height. For the sake of symmetry, we gravitate towards to designing at the center wavelength ($\lambda = 546$ nm) and central field ($\theta_i = 0°$), whose rays are colored in red. Take the central field in channel 2 as an instance and let $\theta_r = 33°$ to secure the total internal reflections for longer visible wavelengths. Then, $\theta_2 = 16.5°$, $p_i = 531.60$ nm, and $h_i = 157.47$ nm. To enhance the reflectivity, on the grating surface is coated a thin film of aluminum [24].

2.5. Out-coupling grating

By way of comparison, the slanted grating [25]—an alternative to the blazed grating—is served as the OCG, whose profile is depicted in Fig. 6. Likewise, the incident angle θ_i, reflected angle θ_r of the first order, grating period p_o, wavelength λ, and refractive index of waveguide n_{wg} shall meet

$$p_o(sin\theta_i - sin\theta_r) = \frac{\lambda}{n_{wg}} \tag{7}$$

To reverse the field back to its original angle, the grating period of OCG should be identical to that of ICG, i.e., $p_o = p_i$. Similar to ICG, a thin film of aluminum shall be deposited onto the surface of OCG as well. This would not just improve the reflectivity, but help to achieve a high (etching) depth-to-width ratio (DWR) that is defined as
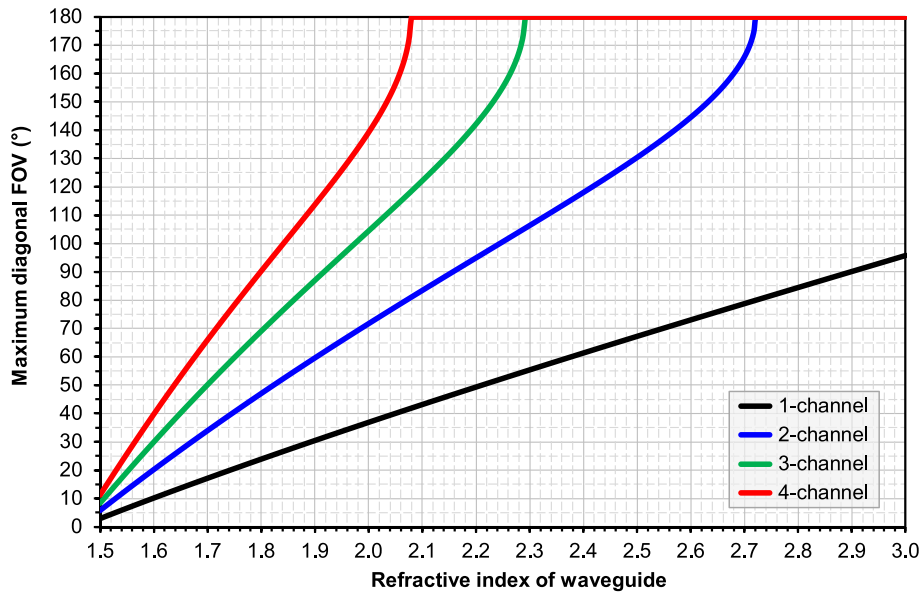
Fig. 4. Maximum diagonal FOV with respect to the refractive index of waveguide, while maintaining the aspect ratio of FOV as 1:1. When $n_{wg} = 1.8858$, the upper limit of FOV is 29°/58°/85°/110° for the single/dual/triple/quad-channel waveguide.
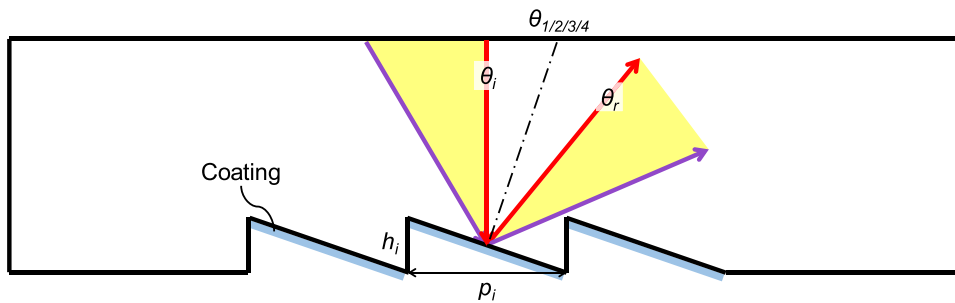

Fig. 5. Profile of in-coupling grating, which is a sawtooth grating. θ_i is the incident angle, θ_r the reflected angle of the first order, $\theta_{1/2/3/4}$ the tilt angle, p_i the grating period, and h_i the grating height.
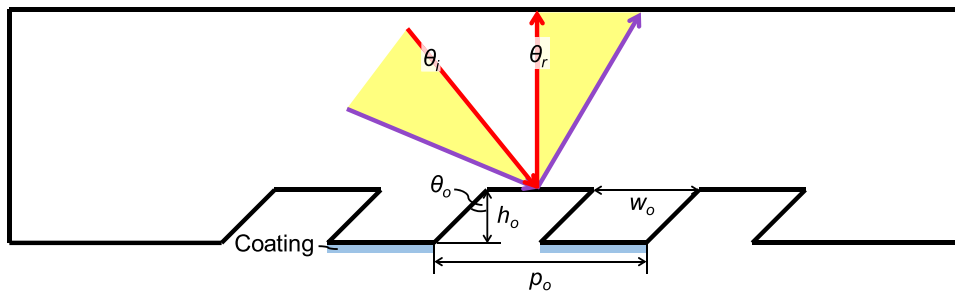

Fig. 6. Profile of out-coupling grating, which is a slanted grating. θ_i is the incident angle, θ_r the reflected angle of the first order, p_o the grating period, w_o the grating width, h_o the grating height, and θ_o the slant angle.

$$DWR = \frac{h_o + d_c}{w_o cos\theta_o} \qquad (8)$$

where h_o is the grating height, d_c the coating thickness, w_o the grating width, and θ_o the slant angle. To modulate the diffraction efficiency (DE), as many as 4 parameters, *i.e.*, h_o, d_c, θ_o, and the fill factor—the ratio of grating width to grating period—can be tweaked.

Table 1
Parameters for the in-coupling grating in channel 2.

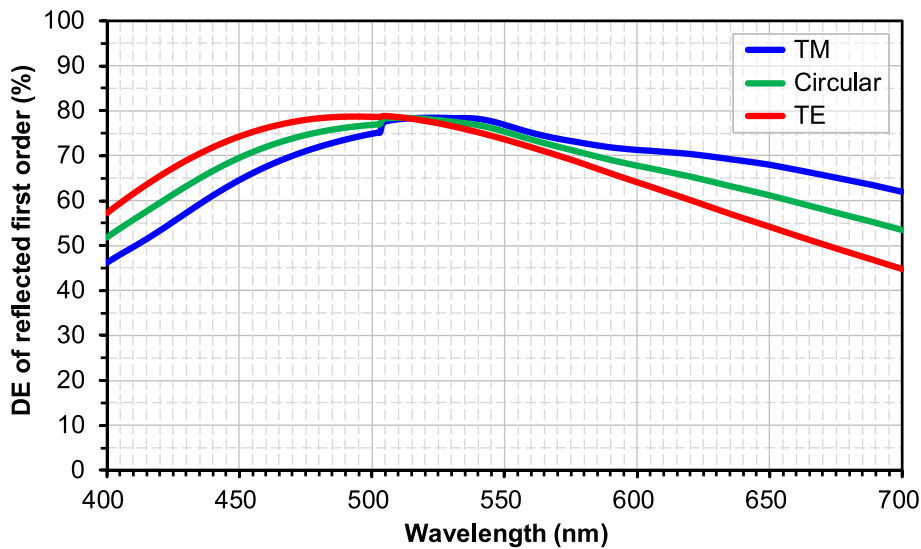| Grating	Shape	Diffraction order	Parameter	Value
In-coupling	Sawtooth	R1	*Base material*	N-LASF31
			Coating material	Aluminum
			p_i	531.60 nm
			h_i	157.47 nm
			θ_2	16.5°
			d_c	36 nm

Fig. 7. DE of the reflected first order of ICG in channel 2 against the wavelength in the visible regime. It can be seen that the DE of circular polarization is 63/76/76 % at 633/546/486 nm, and its spectral bandwidth of DE exceeding 60 % is 235 nm (from 422 nm to 657 nm).

3. Results and discussion

3.1. In-coupling efficiency

By invoking the rigorous coupled-wave analysis (RCWA) method [26], we could conduct numerical calculations of DEs of gratings. For ICG in channel 2, its parameters optimized by the RCWA are listed in Table 1. As shown in Fig. 7, for the transverse magnetic (TM), circular, and transverse electric (TE) polarizations, DEs of reflected first (R1) order of ICG are computed against the wavelengths in the visible regime. As the DE depends sinusoidally on the polarization angle, the DE of circular polarization shall be equal to the average of DEs of TM and TE polarizations [27]. It can be seen that the DE of circular polarization is 63/76/76 % at 633/546/486 nm, and its spectral bandwidth of DE exceeding 60 % is 235 nm (from 422 nm to 657 nm). As shown in Fig. 8, for the TM, circular, and TE polarizations, DEs of R1 order of ICG at 546 nm are computed against the incident angles measured in the waveguide. For the circular polarization, the angular bandwidth of DE exceeding 60 % is 74° (from −17° to +57°). Putting Figs. 7 and 8 together, we could say the sawtooth grating is insensitive to

polarizations. This is a big advantage over polarization-sensitive gratings—*e.g.*, Pancharatnam–Berry grating [28] and chiral liquid crystal grating [29,30]—as we no longer need to worry about the change of polarization, which can be tricky for the light propagating through birefringent and/or scattering media [31]. Plus, the total system efficiency could be doubled by getting rid of the polarizers.

Table 2
Parameters for the out-coupling grating in channel 2.

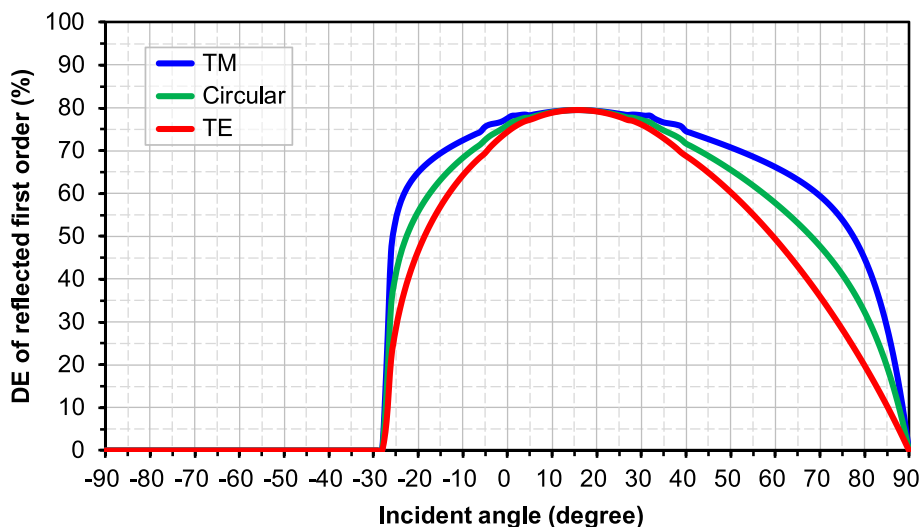| Grating	Shape	Diffraction order	Parameter	Value
Out-coupling	Slanted	R1	*Base material*	N-LASF31
			Coating material	Aluminum
			p_o	531.60 nm
			w_o	265.80 nm
			Fill factor	50 %
			h_o	1073.60 nm
			d_c	21.20 nm
			θ_o	69.72°
			DWR	11.89

Fig. 8. DE of the reflected first order of ICG in channel 2 against the incident angle measured in the waveguide. For the circular polarization, the angular bandwidth of DE exceeding 60 % is 74° (from −17° to +57°).
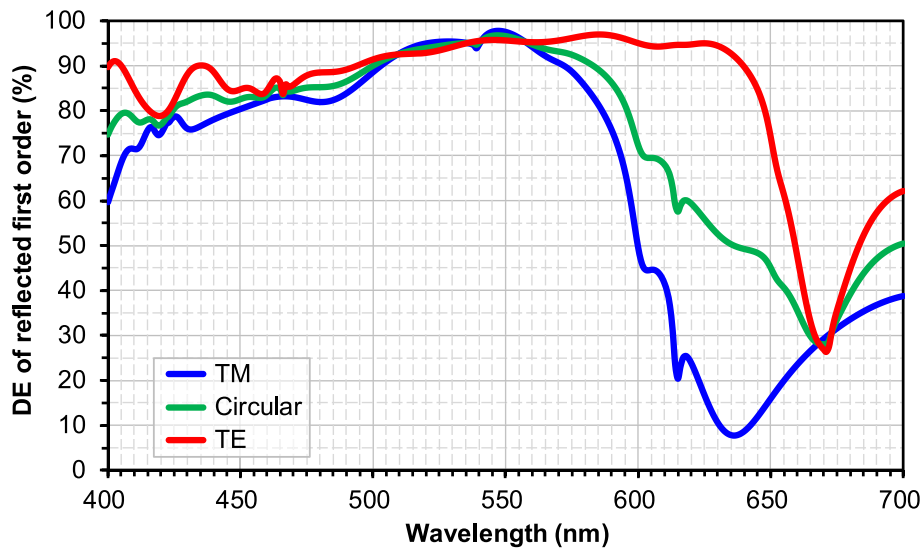
Fig. 9. DE of the reflected first order of OCG in channel 2 against the wavelength in the visible regime. It can be seen that the DE of circular polarization is 51/97/86 % at 633/546/486 nm, and its spectral bandwidth of DE exceeding 60 % is 213 nm (from 400 nm to 613 nm).

3.2. Out-coupling efficiency

For OCG in channel 2, its parameters optimized by the RCWA are listed in Table 2. As shown in Fig. 9, for the TM, circular, and TE polarizations, DEs of R1 order of OCG are computed against the wavelengths in the visible regime. It can be seen that the DE of circular polarization is 51/97/86 % at 633/546/486 nm, and its spectral bandwidth of DE exceeding 60 % is 213 nm (from 400 nm to 613 nm). As shown in Fig. 10, for the TM, circular, and TE polarizations, DEs of R1 order of OCG at 546 nm are computed against the incident angles measured in the waveguide. For the circular polarization, the angular bandwidth of DE exceeding 60 % is 40° (from −37° to +3°). Interestingly, among all polarizations, the TE polarization—which is perpendicular to the grating vector—yields the best performance. As to the modulation of DE, the best practical scheme is to tune the fill factor rather than the grating height, coating thickness, or slant angle. Otherwise, extra processes during the lithography will be incurred. As shown in Fig. 11, for the TM, circular, and TE polarizations, DEs of R1 order of OCG are computed against the fill factor. In agreement with the scalar diffraction theory [32], the DE peaks at the fill factor of 50 %. Compared

to the foregoing sawtooth or blazed grating, the slanted grating is higher in DE, but narrower in both spectral and angular bandwidths and more sensitive to the polarizations.

3.3. Waveguide simulation

The simulation of waveguide is implemented with the light guide toolbox of VirtualLab Fusion. The wavelength is 546 nm. The input FOV in air is 100° (80° (H) × 80° (V)). Correspondingly, the FOV in waveguide is 54° (40° (H) × 40° (V)). Because the FOV in waveguide is equally divided and all angles to be reflected in channel 1/2/3/4 are identical, only the channel 2—where the FOV_2 is located—is demonstrated. The optical setup for our simulation is plotted in Fig. 12, where ten sub-gratings of OCG are labeled from O1 to O10. The thickness D of waveguide is 1.6 mm. The width of ICG shall match with the size of input pupil—a circle with a diameter of 3 mm. The width W_{out} of out-coupling grating is 30 mm, with each sub-grating being 3 mm across. Hence, if the eye relief is 10 mm, exit pupil will be 11.5 × 11.5 mm². The gap between ICG and OCG is 6 mm. The input intensity of the source is normalized to be 1 V²/m². From the ray tracing, the footprints of duplicated pupils of
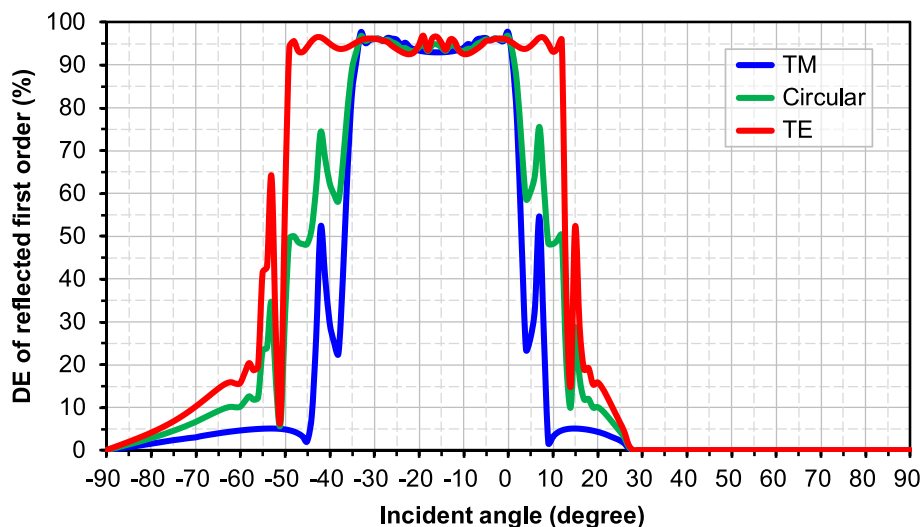

Fig. 10. DE of the reflected first order of OCG in channel 2 against the incident angle measured in the waveguide. For the circular polarization, the angular bandwidth of DE exceeding 60 % is 40° (from −37° to +3°).
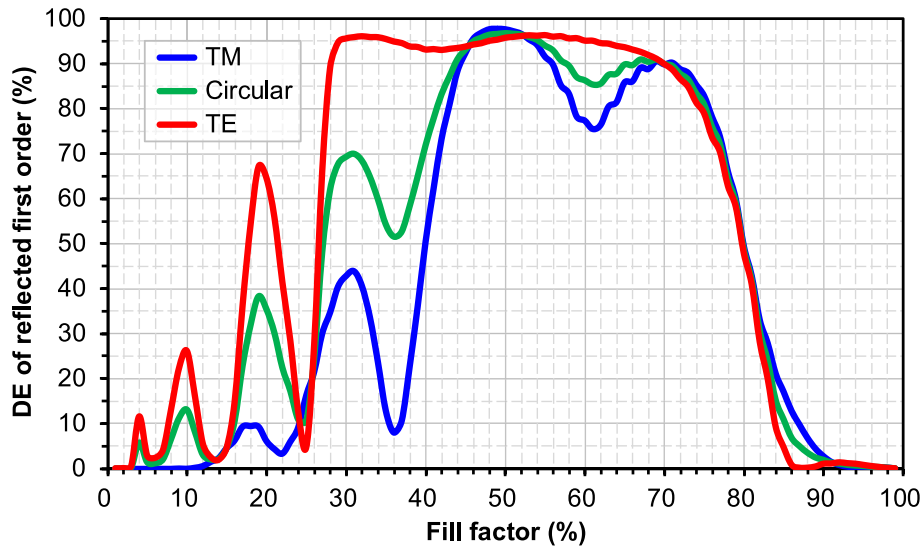
Fig. 11. DE of the reflected first order of OCG in channel 2 against the fill factor. In agreement with the scalar diffraction theory, the DE peaks at the fill factor of 50%.
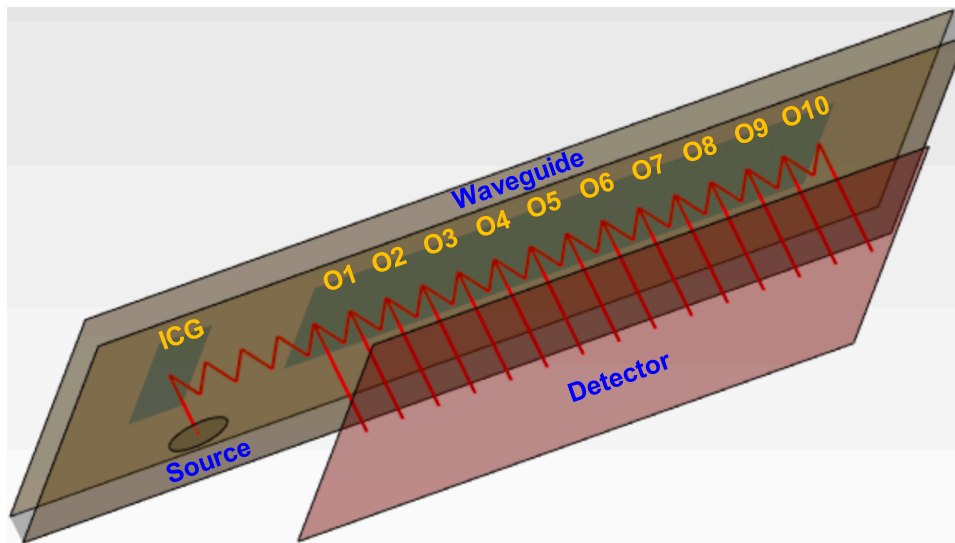

Fig. 12. Optical setup for the simulation on VirtualLab Fusion. Ten sub-gratings of OCG are labeled from O1 to O10. The thickness D of waveguide is 1.6 mm. The width of ICG shall match with the size of input pupil—a circle with a diameter of 3 mm. The width W_{out} of out-coupling grating is 30 mm, with each sub-grating being 3 mm across.

$-19.11°$ (left field of FOV_2), $-9.46°$ (middle field of FOV_2), $0°$ (right field of FOV_2) can be obtained, as shown in Fig. 13. For the overlapped regions of pupils, the coherent summations of electric fields are applied. After the optimization, which is carried out for $0°$ (central field of FOV), the normalized efficiencies of reflected zeroth (R0) and R1 orders are itemized in Table 3. Besides, the intensity, transmittance—the ratio of (minimal intensity I_{min} + maximal intensity I_{max})/2 to input intensity-—and uniformity of three fields are summarized in Table 4. The average transmittance and uniformity are 2.56 % and 75 %, respectively.

4. Conclusions

An ultra-wide-angle NED featuring a quad-channel waveguide has been proposed. Key performance indicators that have been investigated include: FOV is $100°$ (diagonal), eye relief is 10 mm, exit pupil is 11.5×11.5 mm^2, average transmittance is 2.56 %, and average uniformity is 75 %. As a summary, we would like to boil down what we had done into three major contributions. Contribution 1: a change in the mindset about the placement of in-couplers. Instead of placing the in-couplers inside the FOV region, we relocate them to the sub-FOV regions. Contribution 2: one more channel to the FOV division. The multi-channel architectures are coming to the fourth iteration, *i.e.*, quad-channel. Contribution 3: a comparison between the sawtooth grating and slanted grating. Diffraction efficiency and fill factor modulation wise, slanted grating wins. Spectral bandwidth, angular bandwidth and polarization sensitivity wise, sawtooth grating wins. Now that the maximum FOV of quad-channel waveguide is on par with that of magnifier-based NEDs, the magnifier hegemony is no more unshakable. But to completely supersede the magnifiers in the VR headsets, waveguides still have a long road ahead. Other issues, including the low uniformity, chromatic dispersion, stray light, *etc.*, will be dealt with in our future work.
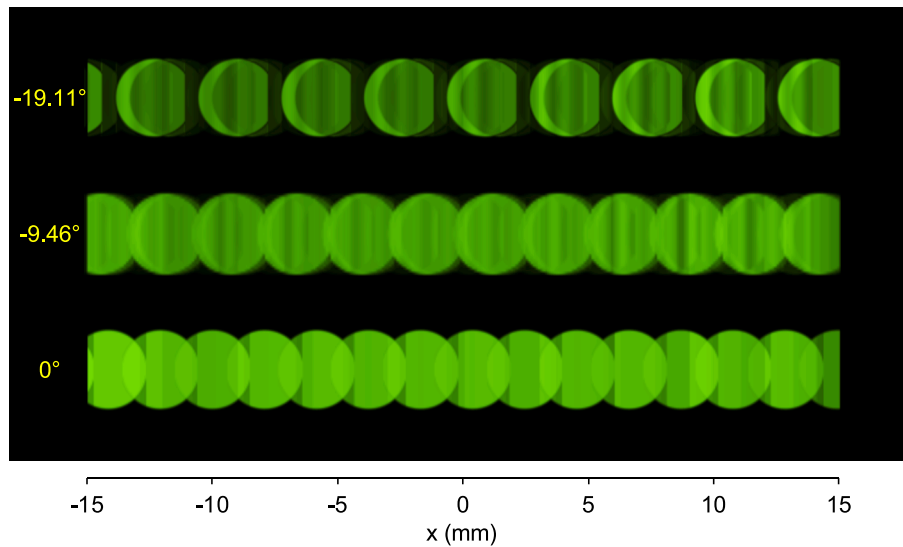
Fig. 13. Footprints and intensities of duplicated pupils of $-19.11°$ (left field of FOV_2), $-9.46°$ (middle field of FOV_2), $0°$ (right field of FOV_2). For the overlapped regions of pupils, the coherent summations of electric fields are applied. The average transmittance and uniformity are 2.56 % and 75 %, respectively.

Table 3
Normalized efficiencies of gratings.

Grating	Efficiency of R0 (%)	Efficiency of R1 (%)
In-coupling	6	94
O1	91.3	8.7
O2	92.8	7.2
O3	91.0	9.0
O4	89.9	10.1
O5	88.4	11.6
O6	86.1	13.9
O7	82.6	17.4
O8	78.3	21.7
O9	67.4	32.6
O10	53.7	46.3

Table 4
Intensity, transmittance and uniformity of left ($-19.11°$), middle ($-9.46°$) and right ($0°$) fields of FOV_2.

Field in air (°)	Field in waveguide (°)	I_{min} (V²/m²)	I_{max} (V²/m²)	Transmittance (%)	Uniformity (%)
-19.11	-10	0.0123	0.0323	2.23	55
-9.46	-5	0.0293	0.0458	3.76	78
0	0	0.0155	0.0182	1.69	92
			Average	2.56	75

CRediT authorship contribution statement

Chao Ping Chen: Conceptualization, Methodology, Formal analysis, Resources, Writing – review & editing, Supervision, Project administration, Funding acquisition. **Xinyu Ma:** Writing – original draft, Formal analysis, Data curation. **Seak Pang Zou:** Visualization, Investigation. **Tingyu Liu:** Formal analysis, Investigation. **Qiang Chu:** Validation. **Haiyang Hu:** Validation. **Yuepeng Cui:** Software, Data curation.

Declaration of Competing Interest

The authors declare that they have no known competing financial interests or personal relationships that could have appeared to influence the work reported in this paper.

Data availability

Data will be made available on request.

References

[1] International Data Corporation, AR & VR headsets market share, https://www.idc.com/promo/arvr (accessed 10 November 2023).
[2] J.E. Melzer, K. Moffitt, Head-Mounted Displays: Designing for the User, McGraw-Hill, New York, 1997.
[3] B.C. Kress, Optical Architectures for Augmented-, Virtual-, and Mixed-Reality Headsets, SPIE, Bellingham, 2020.
[4] J. Zou, Z. Luo, E.n. Zhao, Y.i. Rao, S.-T. Wu, Ultracompact virtual reality system with a Pancharatnam-Berry phase deflector, Opt. Express 30 (22) (2022) 39652–39662.
[5] iNFINITE Production, VR headset database, https://www.infinite.cz/projects/HMD-tester-virtual-reality-headset-database-utility (accessed 10 November 2023).
[6] Y. Amitai, Extremely compact high-performance HMDs based on substrate-guided optical element, in: SID Symposium Digest of Technical Papers, Boston, 2004, pp. 310–313.
[7] T. Levola, Diffractive optics for virtual reality displays, J. Soc. Inf. Disp. 14 (5) (2006) 467–475.
[8] H. Mukawa, K. Akutsu, I. Matsumura, S. Nakano, T. Yoshida, M. Kuwahara, K. Aiki, A full-color eyewear display using planar waveguides with reflection volume holograms, J. Soc. Inf. Disp. 17 (3) (2009) 185–193.
[9] Y. Wu, C.P. Chen, L. Zhou, Y. Li, B. Yu, H. Jin, Design of see-through near-eye display for presbyopia, Opt. Express 25 (8) (2017) 8937–8949.
[10] B.T. Schowengerdt, D. Lin, P. St. Hilaire, Multi-layer diffractive eyepiece, US Patent 2018/0052277 A1, 2017.
[11] J. Ha, J. Kim, Augmented reality optics system with pinpoint mirror, US Patent 2019/0204600 A1, 2017.
[12] D. Grey, S. Talukdar, Exit pupil expanding diffractive optical waveguiding device, US Patent 10,359,635 B2, 2018.
[13] D. Cheng, Q. Wang, L. Wei, X. Wang, L. Zhou, Q. Hou, J. Duan, T. Yang, Y. Wang, Design method of a wide-angle AR display with a single-layer two-dimensional pupil expansion geometrical waveguide, Appl. Opt. 61 (19) (2022) 5813–5822.
[14] B.C. Kress, M. Pace, Holographic optics in planar optical systems for next generation small form factor mixed reality headsets, Light Adv. Manuf. 3 (2022) 771–801.
[15] Y. Weng, Y. Zhang, W. Wang, Y. Gu, C. Wang, R. Wei, L. Zhang, B. Wang, High-efficiency and compact two-dimensional exit pupil expansion design for diffractive waveguide based on polarization volume grating, Opt. Express 31 (4) (2023) 6601–6614.
[16] Z. Liu, D. Wang, H. Gao, M. Li, H. Zhou, C. Zhang, Metasurface-enabled augmented reality display: a review, Adv. Photon. 5 (3) (2023), 034001.

[17] T. Vallius, J. Tervo, Waveguides with extended field of view, US Patent 9,791,703 B1, 2016.

[18] Z. Shi, W.T. Chen, F. Capasso, Wide field-of-view waveguide displays enabled by polarization-dependent metagratings, Proc. SPIE 10676 (2018) 1067615.

[19] C. Yoo, K. Bang, M. Chae, B. Lee, Extended-viewing-angle waveguide near-eye display with a polarization-dependent steering combiner, Opt. Lett. 45 (10) (2020) 2870–2873.

[20] C.P. Chen, Y. Cui, Y.e. Chen, S. Meng, Y. Sun, C. Mao, Q. Chu, Near-eye display with a triple-channel waveguide for metaverse, Opt. Express 30 (17) (2022) 31256–31266.

[21] L. Zhou, C.P. Chen, Y. Wu, Z. Zhang, K. Wang, B. Yu, Y. Li, See-through near-eye displays enabling vision correction, Opt. Express 25 (3) (2017) 2130–2142.

[22] W. Zhang, C.P. Chen, H. Ding, L. Mi, J. Chen, Y. Liu, C. Zhu, See-through near-eye display with built-in prescription and two-dimensional exit pupil expansion, Appl. Sci. 10 (11) (2020) 3901.

[23] C.P. Chen, L. Mi, W. Zhang, J. Ye, G. Li, Wide-field-of-view near-eye display with dual-channel waveguide, Photonics 8 (12) (2021) 557.

[24] C.P. Chen, L. Mi, W. Zhang, J. Ye, G. Li, Waveguide-based near-eye display with dual-channel exit pupil expander, Displays 67 (2021), 101998.

[25] L. Mi, C.P. Chen, Y. Lu, W. Zhang, J. Chen, N. Maitlo, Design of lensless retinal scanning display with diffractive optical element, Opt. Express 27 (15) (2019) 20493–20507.

[26] M.G. Moharam, T.K. Gaylord, Rigorous coupled-wave analysis of planar-grating diffraction, J. Opt. Soc. Am. 71 (7) (1981) 811–818.

[27] M. Collischon, H. Haidner, P. Kipfer, A. Lang, J.T. Sheridan, J. Schwider, N. Streibl, J. Lindolf, Binary blazed reflection gratings, Appl. Opt. 33 (16) (1994) 3572–3577.

[28] C.P. Jisha, S. Nolte, A. Alberucci, Geometric phase in optics: from wavefront manipulation to waveguiding, Laser Photon. Rev. 15 (10) (2021) 2100003.

[29] B.S. Bae, S. Han, S.S. Shin, K. Chen, C.P. Chen, Y. Su, C.G. Jhun, Dual structure of cholesteric liquid crystal device for high reflectance, Electron. Mater. Lett. 9 (6) (2013) 735–740.

[30] I. Nys, M. Stebryte, Y.Y. Ussembayev, J. Beeckman, K. Neyts, Tilted chiral liquid crystal gratings for efficient large-angle diffraction, Adv. Opt. Mater. 7 (22) (2019) 1901364.

[31] Z.-H. He, C.-P. Chen, J.-L. Zhu, Y.-C. Yuan, Y. Li, W. Hu, X. Li, H.-J. Li, J.-G. Lu, Y.-K. Su, Electrically tunable holographic polymer templated blue phase liquid crystal grating, Chin. Phys. B 24 (6) (2015), 064203.

[32] D.C. O'Shea, T.J. Suleski, A.D. Kathman, D.W. Prather, Diffractive Optics: Design, Fabrication, and Test, SPIE, Bellingham, 2004.